

1N-92-CR
 (Emission)

ELECTRON DENSITIES IN SOLAR FLARE LOOPS, CHROMOSPHERIC EVAPORATION UPFLOWS, AND ACCELERATION SITES

MARKUS J. ASCHWANDEN

Department of Astronomy, University of Maryland, College Park, MD 20742; markus@astro.umd.edu

AND

ARNOLD O. BENZ

Institute of Astronomy, ETH Zürich, Haldeliweg 15, ETH-Zentrum, CH-8092 Zürich, Switzerland; benz@astro.phys.ethz.ch

Received 1996 September 4; accepted 1996 December 5

ABSTRACT

We compare electron densities measured at three different locations in solar flares: (1) in soft X-ray (SXR) loops, determined from SXR emission measures and loop diameters from *Yohkoh* Soft X-Ray Telescope maps [$n_e^{\text{SXR}} = (0.2\text{--}2.5) \times 10^{11} \text{ cm}^{-3}$]; (2) in chromospheric evaporation upflows, inferred from plasma frequency cutoffs of decimetric radio bursts detected with the 0.1–3 GHz spectrometer Phoenix of ETH Zürich [$n_e^{\text{upflow}} = (0.3\text{--}11) \times 10^{10} \text{ cm}^{-3}$]; and (3) in acceleration sites, inferred from the plasma frequency at the separatrix between upward-accelerated (type III bursts) and downward-accelerated (reverse-drift bursts) electron beams [$n_e^{\text{acc}} = (0.6\text{--}10) \times 10^9 \text{ cm}^{-3}$].

The comparison of these density measurements, obtained from 44 flare episodes (during 14 different flares), demonstrates the compatibility of flare plasma density diagnostics with SXR and radio methods. The density in the upflowing plasma is found to be somewhat lower than in the filled loops, having ratios in a range $n_e^{\text{upflow}}/n_e^{\text{SXR}} = 0.02\text{--}1.3$, and a factor of 3.6 higher behind the upflow front. The acceleration sites are found to have a much lower density than the SXR-bright flare loops, i.e., $n_e^{\text{acc}}/n_e^{\text{SXR}} = 0.005\text{--}0.13$, and thus must be physically displaced from the SXR-bright flare loops. The scaling law between electron time-of-flight distances l' and loop half-lengths s , i.e., $l'/s = 1.4 \pm 0.3$, recently established by Aschwanden et al. suggests that the centroid of the acceleration region is located above the SXR-bright flare loop, as envisioned in cusp geometries (e.g., in magnetic reconnection models).

Subject headings: acceleration of particles — radiation mechanisms: nonthermal — Sun: corona —

Sun: flares — Sun: X-rays, gamma rays

1. INTRODUCTION

The electron density is one of the fundamental physical parameters characterizing plasma in the solar corona. The plasma of the quiet corona is supposed to be close to thermal equilibrium, and its density thus decreases exponentially with height, at least along open magnetic field lines. Electron beams that propagate through the corona can excite plasma emission, whose frequency is mainly a function of the local electron density and, thus, conveniently traces the density structure along the trajectory. However, deviations from a hydrostatic corona are common, mainly in closed magnetic structures. Heating processes in coronal loops may occur faster than the thermalization time and thus can lead to density scale heights that do not correspond to a thermal equilibrium, and vary with height. During the impulsive phase of flares especially, there is a large departure from equilibrium, with the energizing of the flare plasma resulting in a raising of the electron density as well as temperature. Moreover, chromospheric evaporation is thought to drive an upflow of heated plasma into flare loops, producing steep density gradients at the upflow front. A density diagnostic therefore represents a key tool to probe the various physical processes that evolve during solar flares.

Electron densities in flares can be measured with different methods, employing (1) the plasma frequency of coherent radio emission, (2) the emission measure of soft X-ray (SXR) or X-ray/ultraviolet (XUV) emission, (3) density-sensitive line ratios (in SXRs and the XUV; see, e.g., the review by

Doschek 1990; Phillips 1991), (4) line width measurements of the higher Balmer lines (e.g., Foukal, Miller, & Gilliam 1983), or (5) measurement of the intensity of the electron scattering (white light) continuum for limb flares (e.g., Fisher 1974; Ichimoto et al. 1992). For an extensive review of electron density measurements in flare loops, see Bray et al. (1991, pp. 229–249). In this study we make use of the first two methods in radio and SXR wavelengths, by analyzing radio data from the Phoenix spectrometer (ETH Zürich) and the Soft X-Ray Telescope (SXT) on board the *Yohkoh* spacecraft. The new aspect of this investigation is to compare the electron densities inferred from decimetric radio bursts with those obtained from SXR emission measure maps of flare loops. This intercomparison should lead us to a conclusion whether electron beams that produce decimetric plasma emission propagate inside SXR-bright flare loops or outside, in a volume with lower density. Since the electron density of the acceleration site can be measured from broadband radio spectra that show bidirectional electron beams (accelerated in upward and downward directions), the comparison of its electron density with that of the SXR-bright flare loop should also reveal whether the acceleration site is located inside or outside the SXR flare loop. These observational constraints may have incisive implications for flare models, e.g., whether particle acceleration takes place in DC electric fields inside flare loops versus magnetic reconnection above flare loops. A further spin-off of this study is to probe the electron density in plasma upflows produced by chromospheric evapo-

ration, which is believed to affect crucially the opacity of decimetric radio bursts (Aschwanden & Benz 1995). The radio-inferred values of the electron densities in chromospheric upflows can then be compared with the SXR-inferred values of the filled flare loops, providing a compatibility test of both methods, as well as a tool to monitor the density evolution of filling and already filled-up flare loops.

In § 2, we describe the observations and data analysis in SXR (§ 2.2) and radio (§ 2.3) wavelengths. The interpretation and theoretical modeling of the observational results are discussed in § 3. The conclusions are summarized in § 4.

2. DATA ANALYSIS

2.1. Data Selection

Since our study requires simultaneous density measurements in soft X-rays and radio frequencies, we first select all flare events that have been commonly observed with the *Yohkoh* SXT in flare mode and with the broadband radio spectrometer Phoenix of ETH Zürich. This selection criterion produces a catalog of 29 common flares between 1992 July and 1993 December. We omit observations with incomplete frequency coverage over the 100–3000 MHz range (six events) or with incomplete time coverage by SXT (two events). From the remaining 21 events, we identify radio bursts in the 0.1–3.0 GHz frequency range during 14 flares (67%) recorded with SXT in flare mode, while no radio bursts were detected in seven flares (33%) over the entire frequency range. The radio/SXR association rate found here (67%) is marginally lower than the radio/hard X-ray (HXR) association rate (85%; Simnett & Benz 1986). The fact that no H α emission was reported (NOAA Solar-Geophysical Data Bulletin) in five of the seven radio-quiet flares may indicate that they correspond to rather weak flares. In this study we focus on the data set with 14 flares simultaneously detected in both SXRs and radio emission, while the remaining data set with “radio quiet” SXR flares will be investigated in a separate study. The list of the 14 analyzed flares is presented in Table 1.

2.2. Soft X-Ray Data Analysis from *Yohkoh* SXT

The Soft X-Ray Telescope on board the *Yohkoh* spacecraft is a grazing-incidence reflecting telescope of 1.5 m focal length that employs a 1024×1024 format virtual-phase CCD detector with an angular resolution of $2''.45$ (Tsuneta et al. 1991). Once a flare trigger is activated, SXT records a set of images for each episode from the flare region in a limited field of view with 64×64 pixels, with a cadence of a few seconds per filter, usually cycling through a sequence of four different filters (1265 Å Al, 2930 Å Al + 2070 Å Mg, 11.6 μ m Al, and 119 μ m Be), which are sensitive in wavelength ranges from 2.5–36 Å (thin Al filter) to 2.3–10 Å (Be filter).

Depending on the flare duration, SXT records up to ≈ 1000 images per flare. The selection of SXT images in our analysis is dictated by the occurrence time of decimetric radio bursts. Therefore we select, for each episode of decimetric radio bursts, the SXT images that are most nearly coincident, these varying in number between one image per flare (for flares with short radio coverage or flare duration of $\lesssim 1$ minute) and a maximum of 15 images per flare (for the longest flare, with radio coverage over ≈ 30 minutes). The total number of observed radio burst episodes amounts

to 44 during 14 different flares. For each radio episode, we analyze two SXT images with different filters and determine from the filter ratio an emission measure (EM) map and an electron temperature (T_e) map, using the standard *Yohkoh* software (see IDL procedures SXT-PREP and SXT-TEEM), described in Morrison (1994). The time interval between a pair of SXT images used for filter ratios is always less than a few seconds. The derivation of temperature and emission measure from filter ratios is based on emission-line spectra computed by Mewe, Gronenschild, & van den Oord (1985), using coronal abundances, and on continuum spectra computed by Mewe, Lemen, & van den Oord (1986).

Starting from the emission measure maps, which are a measure of the squared electron density integrated along the line of sight, we estimate the column depth of the line of sight from the transverse diameters of apparent SXR loops. This approach is fairly safe for flare loops that show unambiguous single-loop structures (sometimes corroborated by the position of conjugate HXR double footpoints) and may serve as a first approximation for less unambiguous cases. Figure 1 shows an example of how the diameter of a flare loop is measured. From three different scans extracted perpendicular to the flare loop, we determine the full width at half-maximum (FWHM) of the emission measure profile, $EM(x)$, on a linear scale. Assuming a constant electron density n_e across the circular loop cross section, we approximate the emission measure profile by

$$EM(x) = \int n_e^2 dh(x) \approx n_e^2 2r \sqrt{1 - (x/r)^2}, \quad (1)$$

with r the radius of the flare loop. The FWHM of this semicircular function is related to the radius r by $FWHM = r\sqrt{3}$. Thus, interpolating a semicircular function through the maximum and the two FWHM points, we find with equation (1) a unique value for the electron density n_e^{SXR} at each given scan of the SXR flare loop. The example in Figure 1 shows that the loop diameter $d = 2r$ varies between 6.0 and 9.5 Mm for the three scans of this particular flare loop while the electron density varies in the range $n_e^{SXR} = (1.5\text{--}1.9) \times 10^{11} \text{ cm}^{-3}$. The viability of this approach should be judged from the goodness of fit of the model (eq. [1]). The example in Figure 1 (and most of the other analyzed cases) shows an acceptable agreement with the model, except for tails at a level of $\lesssim 20\%$ of the peak emission measure. The tails may indicate a lower electron density in the surrounding volume of the flare loop or may partially be caused by the point-spread function of the SXT, which is characterized by a Moffat function (Martens, Acton, & Lemen 1995).

We determine in this way the electron density n_e^{SXR} of SXR flare loops for all 44 flare episodes during decimetric radio bursts. Figure 2 shows the brightest SXT image for each of the 14 flares. The three scans per flare were chosen close to the location of the peak emission measure, which is the most likely place for flare activity in an SXR image, because the highest density is produced where the highest plasma pressure is built up during the flare, while flare-unrelated SXR emission (e.g., from postflare loops from previous flares) is expected to have generally a lower density. The loop structure is not always obvious in the SXT images shown in Figure 2 (e.g., flares 4, 6), and barely resolved (e.g., flares 6, 14) and double loops are present (e.g., flares 7, 11). To facilitate judgment of the magnetic conjugacy of loop footpoint positions, we overlay also the magnetic inversion

TABLE 1
MEASUREMENTS OF ELECTRON DENSITIES IN 14 SOLAR FLARES

EVENT	TIME (UT)	BURST TYPE ^a	FREQUENCY (MHz)			DENSITY (cm ⁻³)			DIAMETER <i>d</i> (Mm)	DENSITY RATIO	
			ν^{III}	$\nu^{\text{dm},1}$	$\nu^{\text{dm},2}$	$n_e^{\text{III}} (\times 10^9)$	$n_e^{\text{dm},2} (\times 10^{11})$	$n_e^{\text{SXR}} (\times 10^{11})$		q^{III}	$q^{\text{dm},2}$
92 Sep 5:											
1a	1123:42	dm-Puls	520	1050	2150	3.4	0.57	1.37	5.0	0.024	0.42
1b	1123:51	dm-RS	530	2000	3000	3.5	1.12	1.37	5.0	0.025	0.81
1c	1125:38	dm-Puls	550	1010	1950	3.8	0.47	1.37	5.4	0.027	0.34
1d	1126:48	dm-Cont	650	1050	1950	5.2	0.47	1.48	7.8	0.035	0.32
1e	1127:03	dm-Cont	650	650	1730	5.2	0.37	1.76	5.4	0.030	0.21
1f	1129:12	dm-Cont	530	1070	1600	3.5	0.32	2.54	6.0	0.014	0.12
92 Sep 6:											
2a	0903:42	dm-RS	...	1010	2030	...	0.51	1.59	4.6	...	0.32
3a	1147:57	dm-RS	330	550	860	1.4	0.09	0.85	5.6	0.016	0.11
3b	1149:51	dm-Puls	...	2030	2970	...	1.09	1.66	4.6	...	0.66
3c	1151:05	dm-Cont	...	860	1500	...	0.28	1.46	6.8	...	0.19
3d	1153:45	dm-RS	620	620	1440	4.8	0.26	1.92	8.2	0.025	0.13
3e	1155:39	dm-RS	340	1560	2970	1.4	1.09	2.16	7.8	0.007	0.51
3f	1156:27	dm-Puls	360	1070	1840	1.6	0.42	1.98	8.2	0.008	0.21
3g	1157:46	dm-Puls	330	830	1800	1.4	0.40	2.14	8.6	0.006	0.19
3h	1201:49	dm-Puls	...	810	1470	...	0.27	1.80	8.4	...	0.15
3i	1205:27	dm-Cont	320	1070	1500	1.3	0.28	2.25	7.6	0.006	0.12
3j	1207:59	dm-Puls	...	810	1950	...	0.47	2.19	8.2	...	0.22
3k	1209:02	dm-Puls	...	810	1660	...	0.34	2.24	6.4	...	0.15
3l	1209:27	dm-RS	...	1530	2380	...	0.70	2.24	6.4	...	0.31
3m	1210:33	dm-Cont	...	910	1500	...	0.28	2.24	6.4	...	0.12
3n	1212:32	dm-RS	...	890	1560	...	0.30	2.38	7.8	...	0.13
3o	1216:05	dm-RS	280	520	1660	1.0	0.34	2.00	10.0	0.005	0.17
92 Sep 7:											
4a	0711:20	dm-RS	...	760	1440	...	0.26	0.37	11.2	...	0.69
5a	0742:29	dm-RS	...	840	1360	...	0.23	0.25	14.6	...	0.92
5b	0742:43	dm-RS	...	910	1760	...	0.38	0.20	18.4	...	1.92
6a	0849:28	dm-RS	...	720	1210	...	0.18	0.55	3.4	...	0.33
92 Sep 12:											
7a	1539:57	dm-Cont	730	730	2110	6.6	0.55	0.52	6.0	0.127	1.06
92 Oct 5:											
8a	0923:49	dm-Puls	220	810	2030	0.6	0.51	0.78	6.2	0.008	0.66
8b	0924:41	dm-Puls	260	610	2030	0.8	0.51	1.13	6.4	0.007	0.45
93 Jan 18:											
9a	1301:12	dm-Puls	...	1090	2330	...	0.67	0.49	8.6	...	1.37
93 Oct 2:											
10a	0739:48	dm-Puls	450	460	2740	2.5	0.93	0.60	4.2	0.042	1.55
10b	0741:34	dm-Puls	810	810	1910	8.1	0.45	0.81	6.4	0.100	0.56
10c	0744:37	dm-Cont	910	910	1910	10.3	0.45	0.81	5.4	0.127	0.56
10d	0744:42	dm-RS	640	1870	2970	5.1	1.09	0.81	5.4	0.063	1.35
93 Oct 3:											
11a	0924:49	dm-Cont	440	1840	2530	2.4	0.79	0.33	6.0	0.073	2.41
11b	0925:17	dm-Cont	380	640	1390	1.8	0.24	0.33	6.0	0.054	0.73
11c	0927:22	dm-RS	...	1180	1630	...	0.33	0.32	13.6	...	1.03
12a	1242:43	dm-Cont	340	1530	2850	1.4	1.01	0.33	4.6	0.043	3.05
12b	1242:37	dm-RS	360	360	500	1.6	0.03	0.33	4.6	0.049	0.09
12c	1245:35	dm-RS	...	1500	2150	...	0.57	0.49	6.4	...	1.17
93 Oct 20:											
13a	0954:40	dm-IV	...	330	1420	...	0.25	0.42	11.8	...	0.60
13b	0956:00	dm-IV	...	360	1470	...	0.27	0.77	8.4	...	0.35
13c	0958:22	dm-IV	...	320	1160	...	0.17	0.79	11.4	...	0.21
93 Dec 1:											
14a	1112:52	dm-RS	750	750	1050	7.0	0.14	0.75	8.4	0.093	0.18

^a See § 2.3.

(neutral) line in Figure 2 (*dotted contours*). The measured values of the peak electron density n_e^{SXR} and loop diameter d are listed in Table 1, while histograms of these and the emission measures are shown in Figure 3. The SXR peak emission measure values range from $\text{EM} = 4 \times 10^{29} \text{ cm}^{-5}$ to $\text{EM} = 1 \times 10^{32} \text{ cm}^{-5}$. The loop diameters vary from $d = 3400$ to $d = 18,400$ km, and the corresponding peak electron densities from $n_e^{\text{SXR}} = 0.2 \times 10^{11}$ to $n_e^{\text{SXR}} = 2.5 \times 10^{11} \text{ cm}^{-3}$.

The electron temperatures inferred from the SXT images at the locations of the emission measure maximum (with a

mean and standard deviation of $\log \text{EM} = 47.1 \pm 0.7$ per SXT pixel) vary over the relatively small range $T_e = 9.3 \pm 1.6$ MK, with extremal values of 7.3 and 14.1 MK. These SXT flare temperatures seem to be typically a factor of 2 lower than those inferred from Ca xix lines with the Bragg Crystal Spectrometer. For instance, for the 1992 September 6, 0903 UT flare, we find $T_e^{\text{SXT}} = 9.5$ MK while Ca xix measurements yield $T_e^{\text{BCS}} = 20$ MK (Zarro, Mariska, & Dennis 1994) at the flare peak, and for the 1992 September 12, 1539 UT flare we find $T_e^{\text{SXT}} = 8.6$ MK while Ca xix measurements yield $T_e^{\text{BCS}} = 14$ MK (Ding et al. 1996). Thus

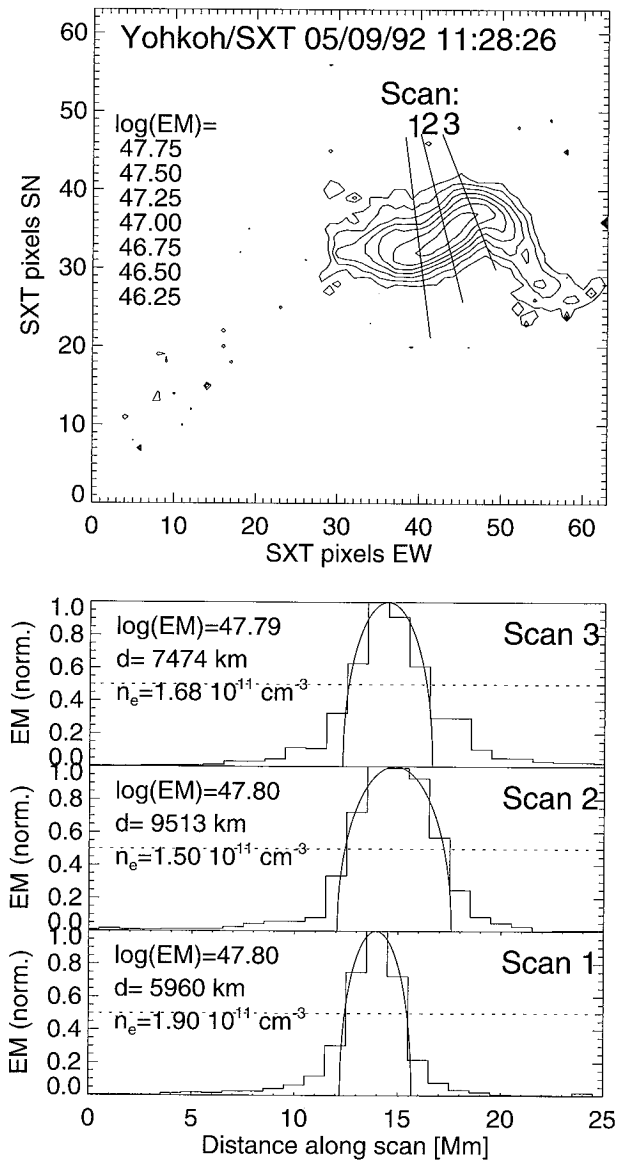


FIG. 1.—Measurement of the electron density n_e from a Yohkoh SXT emission measure (EM) map (top). One-dimensional scans are extracted perpendicular to the flare loop (labeled 1, 2, and 3), and the FWHM of the linear EM along the scans is measured (bottom). The bins indicate the SXT resolution of $2''.45$, and the smooth curve interpolated through the maximum and the two sides at half-maximum indicates the density profile expected for a circular cross section with constant density. The maximum of the emission measure [$\log(\text{EM}) \times \text{SXT pixel area}$], the loop diameter (d), and the measured electron density (n_e) are listed on the left for each scan.

the SXR measurements do not refer to the hottest parts of the flare loops, or do not properly resolve the temperature as a result of unresolved filling factors that enter the filter ratios.

2.3. Radio Data Analysis from Phoenix

The main purpose of this study is to compare the electron density inferred from SXR emission measures with the radio-inferred values, based on the plasma frequency of decimetric radio bursts. Therefore we identify flare episodes with decimetric (0.3–3.0 GHz) radio bursts and determine their radio spectra during these time intervals. From these spectra we determine the low- and high-frequency cutoffs,

to constrain lower and upper limits of the plasma frequency and the corresponding electron density in the radio source.

Phoenix is a digital radio spectrometer at ETH Zürich, sampling dynamic spectra with a typical time resolution of 100 ms and with a frequency resolution of 15 MHz over the frequency range from 100 to 3000 MHz. A description of the instrument is provided in Benz et al. (1991). The 14 SXT flares analyzed in this study were all recorded with a frequency resolution of 15 MHz in the 1.0–3.0 GHz range, and with somewhat coarser frequency steps in the 0.1–1.0 GHz range, because of gaps caused by terrestrial interference. The data quality can be considered as excellent, thanks to the improved antenna-tracking system implemented in 1991. The radio spectrum is found to be stable over the entire 0.1–3.0 GHz range within a few solar flux units after calibration and preflare background subtraction (see rms amplitude of background in Figs. 4–6 and in spectra of Fig. 7).

For the identification and classification of decimetric radio bursts (also called DCIMs), we follow the nomenclature previously established from representative surveys of decimetric radio bursts observed by the ETH Zürich radio telescopes, by means of analog spectra in the 0.3–1.0 GHz range (Wiehl, Benz, & Aschwanden 1985), digital spectra in the 0.3–1.0 GHz range (Güdel & Benz 1988), and digital spectra in the 1–3 GHz range (Islaker & Benz 1994). Based on the morphological definitions in these three catalogs, we subdivide the observed decimetric events into (1) *decimetric type III (dm-III) or reverse-slope (dm-RS) drift bursts* (see examples in Fig. 4, showing detached narrowband or broadband fast-drift bursts, with measurable or almost infinite drift rates and typical durations of $\lesssim 1$ s), (2) *decimetric pulsations (dm-Puls)* (see examples in Fig. 5, showing coherent, quasi-periodic sequences of fast-drifting structures with pulsed time structures of $\lesssim 1$ s, usually bound by a constant or slowly drifting low- and high-frequency cutoff), and (3) *decimetric diffuse continua (dm-Cont)* (see examples in Fig. 6, showing diffuse “patches” in frequency and time, lasting for several seconds, i.e., significantly shorter than type IV events). The classification of the burst types in the 44 events is listed in Table 1.

In our analysis of the 44 decimetric bursts, we determine the background-subtracted radio spectra in the 0.1–3.0 GHz range (each shown in Fig. 7) and measure the low- and high-frequency cutoffs of each decimetric burst, listed as $\nu_{\text{dm},1}^{\text{dm}}$ and $\nu_{\text{dm},2}^{\text{dm}}$ in Table 1. The measured frequencies refer to the selected, time-coherent burst groups identified in the dynamic spectra, while occasionally superposed minor bursts with different spectra were ignored. Multiple spectral peaks in the spectra shown in Figure 7 often indicate multiple structures in time rather than in frequency, having their spectral peaks at slightly different frequencies. The spectral ranges of the selected dominant burst groups are indicated with hatched areas in Figure 7, while other spectral enhancements belong to accidentally superposed other burst types. For each flare we also monitored metric type III bursts, but we detected them in only 25 of the 44 analyzed flare episodes. Whenever observed, we measured the start frequency of metric type III bursts from the spectra shown in Figure 7, listed as $\nu_{\text{III}}^{\text{III}}$ in Table 1. Several cases also show decimetric RS bursts simultaneously during metric type III bursts, where the average type III start frequency was found to be roughly coincident with the separatrix frequency between the two oppositely drifting burst types

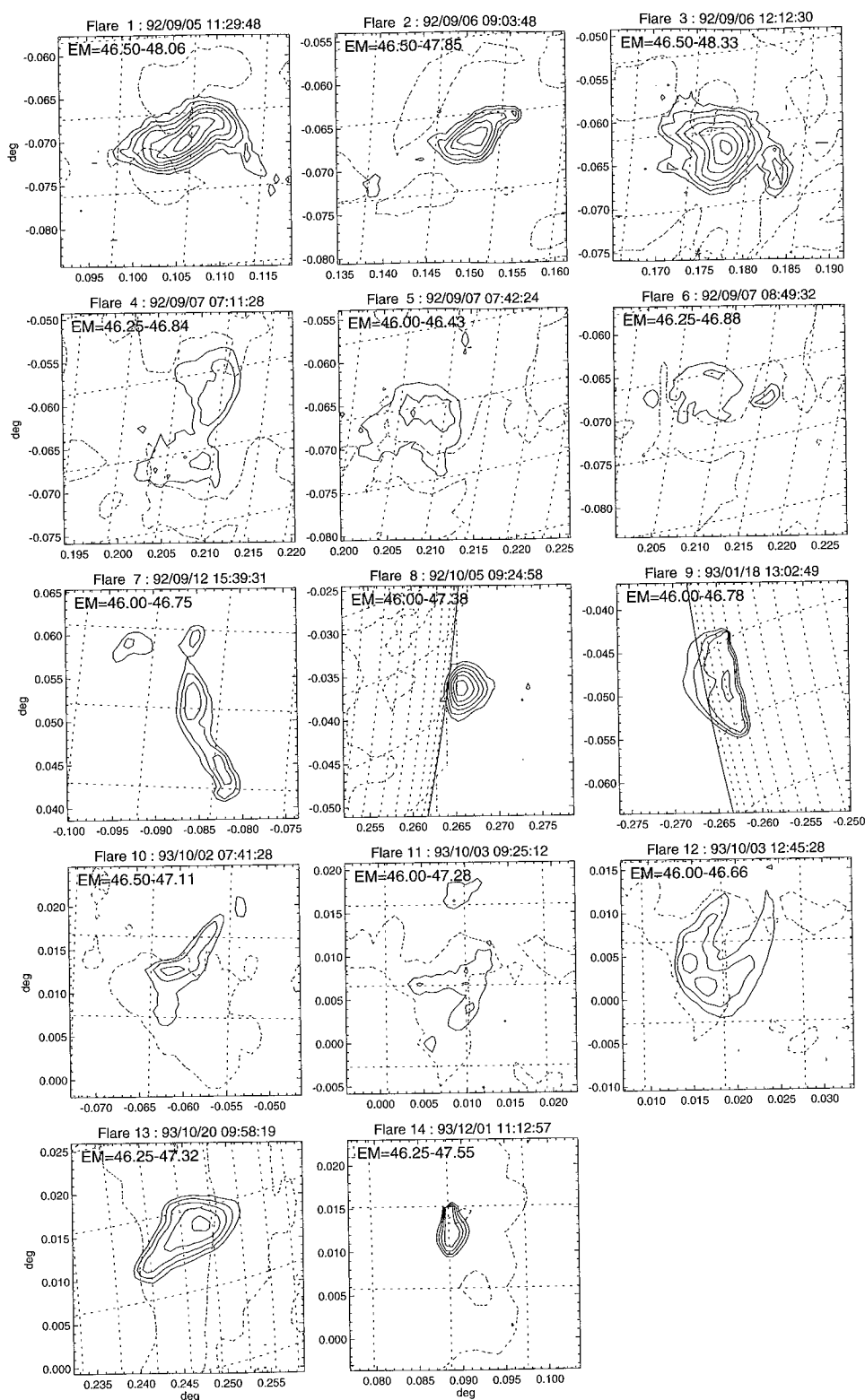


FIG. 2.—Logarithmic emission measure maps of the 14 analyzed flares, observed by the *Yohkoh* SXT. The logarithmic contours are in steps of 0.25 (with the contour level range indicated at the top of each panel). A heliographic grid with a spacing of 2° (24,300 km) is overlaid to indicate the extent and heliographic position. The axis labels indicate the position relative to solar center (in R.A./decl. degrees aligned to the solar axis). The flare number, date, and time are indicated above each panel. The times of the images were chosen near the peak time of the emission measure. The magnetic neutral line, obtained from KPNO magnetograms (with $4''$ resolution) and rotated to identical times of the SXT images, is drawn with dotted lines.

(two cases are studied in detail in Aschwanden, Benz, & Schwartz 1993). The distributions of these measured frequencies are shown in Figure 8, and the ranges and mean values are listed in Table 2.

In a next step, we convert the measured radio frequencies ν^{III} , $\nu^{\text{dm},1}$, and $\nu^{\text{dm},2}$ into approximate values of electron densities, i.e., n_e^{III} , $n_e^{\text{dm},1}$, and $n_e^{\text{dm},2}$, by setting the observed radio frequency equal to the fundamental electron plasma

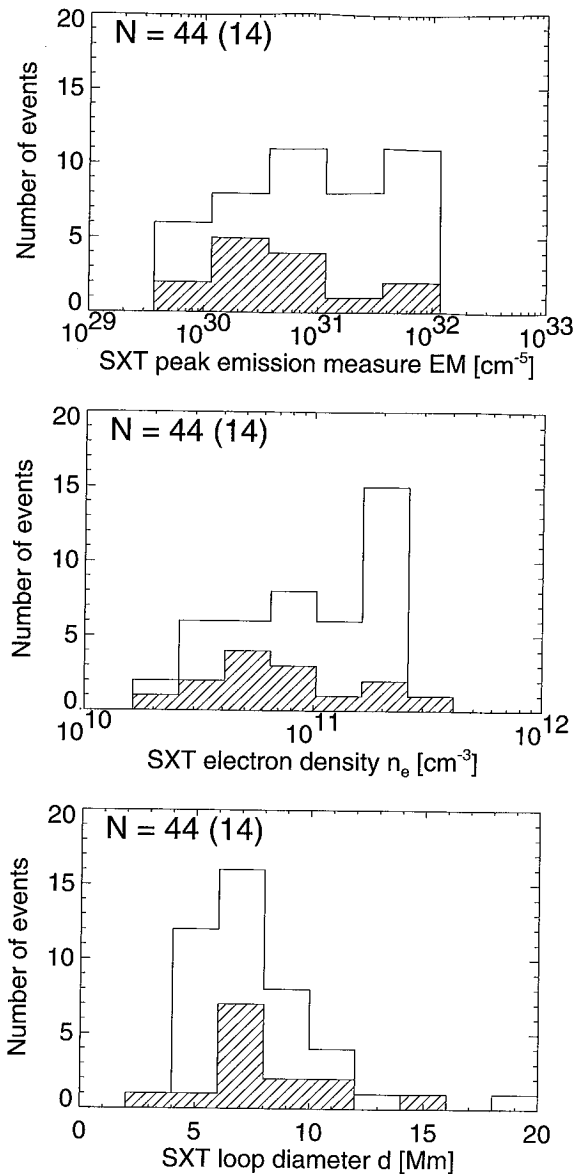


FIG. 3.—Statistics of the SXT peak emission measure values (top), the measured electron densities n_e (middle), and loop diameters d (bottom), for all 44 analyzed flare episodes (open histograms) and for the peak times of each of the 14 flares (hatched histograms).

frequency ν_p ,

$$\nu_p = \sqrt{\frac{n_e e^2}{\pi m_e}} = 8980 \sqrt{n_e} \text{ (Hz)}, \quad (2)$$

with n_e the electron density, e the elementary charge of an electron, and m_e the electron mass (in cgs units). Implicitly it is assumed that the observed metric and decimetric radio emission is related to fundamental plasma emission. The justification for this assumption is discussed in § 3.2. If some bursts were emitted at the harmonic level of the plasma frequency, the inferred density would be a factor of 4 lower. The conversion into electron densities allows us to make comparisons with SXR-inferred densities n_e^{SXR} in flare loops (see hatched areas overlaid on the spectra in Fig. 7 and histograms in the middle column of Fig. 8). The ratios of radio-inferred to SXR-inferred electron densities, i.e., $q = n_e^{\text{radio}}/n_e^{\text{SXR}}$, are compiled in Table 2 (see also distributions in the right column of Fig. 8).

3. DISCUSSION

3.1. SXR Density Diagnostics

From our sample of radio-selected flare episodes, we found electron densities in SXR-bright flare loops in the range $n_e^{\text{SXR}} = (0.2\text{--}2.5) \times 10^{11} \text{ cm}^{-3}$. These values are in good agreement with previous studies using the same method ($\text{EM} = \int n_e^2 dV$): e.g., $n_e^{\text{SXR}} = (0.13\text{--}1.9) \times 10^{11} \text{ cm}^{-3}$ for a data set of 25 compact flare loops observed with *Skylab* (Pallavicini, Serio, & Vaiana 1977). For localized bright loop tops in four flares observed with *Yohkoh*, somewhat higher electron densities ($n_e^{\text{SXR}} = 2.9 \times 10^{11}$ to $1.2 \times 10^{12} \text{ cm}^{-3}$) have been measured (Doschek 1994; Doschek, Strong, & Tsuneta 1995). Comparing with the density diagnostic from SXR line ratios, using the ratio of the forbidden to intercombination lines for He-like ions (Gabriel & Jordan 1972; Brown & Nakagawa 1978), comparable densities were reported (e.g., $n_e = 3 \times 10^{10} \text{ cm}^{-3}$, Brown et al. 1986; $n_e = 10^{11} \text{ cm}^{-3}$, McKenzie et al. 1980), but also significantly higher values, e.g., $n_e > 10^{12} \text{ cm}^{-3}$ (Doschek et al. 1981; Linford & Wolfson 1988), so that the density range in typical flares covers a wider range, from a few times 10^{10} cm^{-3} to several times 10^{12} cm^{-3} (Doschek 1990). Extremely high electron densities of $n_e = 2 \times 10^{12}$ to $1 \times 10^{13} \text{ cm}^{-3}$ have been recently reported by Phillips et al.

TABLE 2
STATISTICS OF FREQUENCY AND ELECTRON DENSITY MEASUREMENTS

Parameter	Range	Mean and Standard Deviation
Frequency (MHz):		
Type III start, ν^{III}	220–910	490 ± 190
Decimetric low, $\nu^{\text{dm},1}$	320–2030	960 ± 440
Decimetric high, $\nu^{\text{dm},2}$	500–3030	1850 ± 580
SXR loop plasma, ν^{SXR}	1270–4526	2960 ± 1010
Electron density (cm^{-3}):		
In acceleration site, $n_e^{\text{acc}} \approx n_e^{\text{III}}$	$(0.6\text{--}10.2) \times 10^9$	$(3.4 \pm 2.5) \times 10^9$
In upflow front, $n_e^{\text{upflow},1} \approx n_e^{\text{dm},1}$	$(0.13\text{--}5.1) \times 10^{10}$	$(1.3 \pm 1.3) \times 10^{10}$
In bulk upflow, $n_e^{\text{upflow},2} \approx n_e^{\text{dm},2}$	$(0.3\text{--}11.2) \times 10^{10}$	$(4.7 \pm 2.9) \times 10^{10}$
In SXR loop, n_e^{SXR}	$(0.2\text{--}2.5) \times 10^{11}$	$(1.2 \pm 0.8) \times 10^{11}$
Electron density ratio:		
$q^{\text{acc}} = n_e^{\text{acc}}/n_e^{\text{SXR}}$	0.005–0.127	0.027 ^a
$q^{\text{upflow},1} = n_e^{\text{upflow},1}/n_e^{\text{SXR}}$	0.016–1.27	0.09 ^a
$q^{\text{upflow},2} = n_e^{\text{upflow},2}/n_e^{\text{SXR}}$	0.09–3.05	0.35 ^a
$Q^{\text{upflow}} = n_e^{\text{upflow},2}/n_e^{\text{upflow},1}$	1.9–35.5	3.6 ^a

^a Median value.

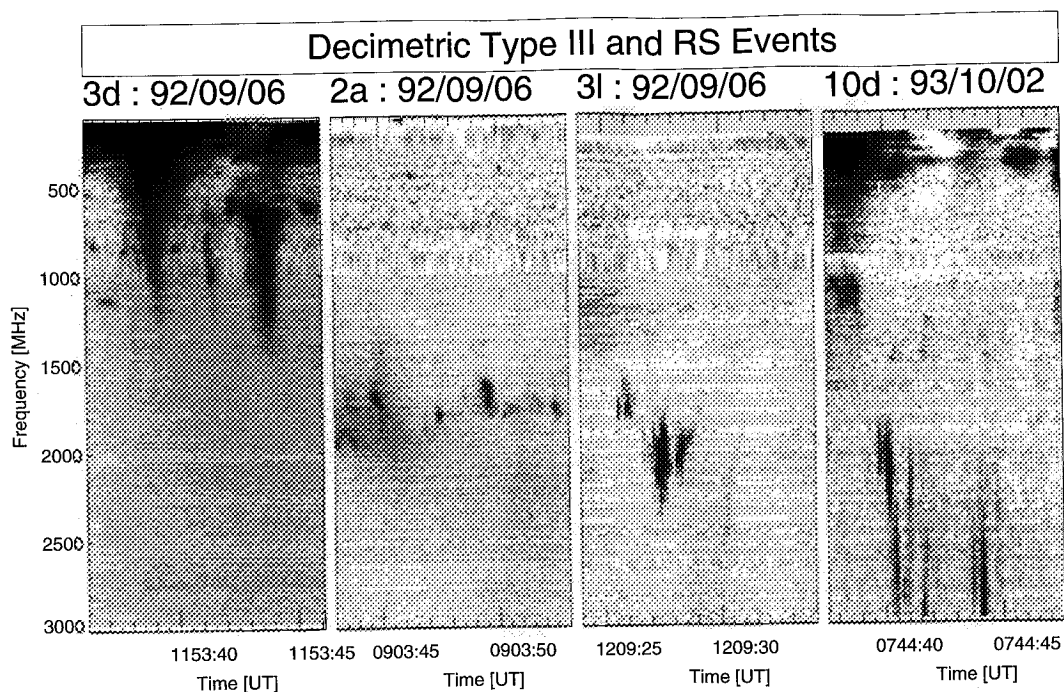


FIG. 4.—Dynamic spectra of radio bursts recorded by Phoenix of ETH Zürich, with four examples of decimetric reverse-slope (RS) burst events. All panels in Figs. 4–6 are shown on the same frequency scale (100–3000 MHz) and on the same timescale (10 s per frame), to facilitate comparisons of burst frequencies, bandwidths, timescales, and radio-quiet frequencies. The radio flux is shown on a logarithmic scale, with a background spectrum subtracted; dark colors indicate enhanced emission. The time resolution is 100 ms. The frequency resolution is 15 MHz, and some noisy frequencies with interference have been interpolated.

(1996), based on new calculations of Fe xxI and Fe xxII intensities. Such extremely high electron densities imply very rapid radiative cooling rates (≈ 1.4 s) and require strong magnetic fields ($B \approx 500$ G) for confinement. If the

measurements were cospatial, the systematically higher values obtained from SXR line ratios would imply low filling factors (≈ 0.01 – 0.10) inside flare loops, in order to reconcile the lower values obtained from the spatially aver-

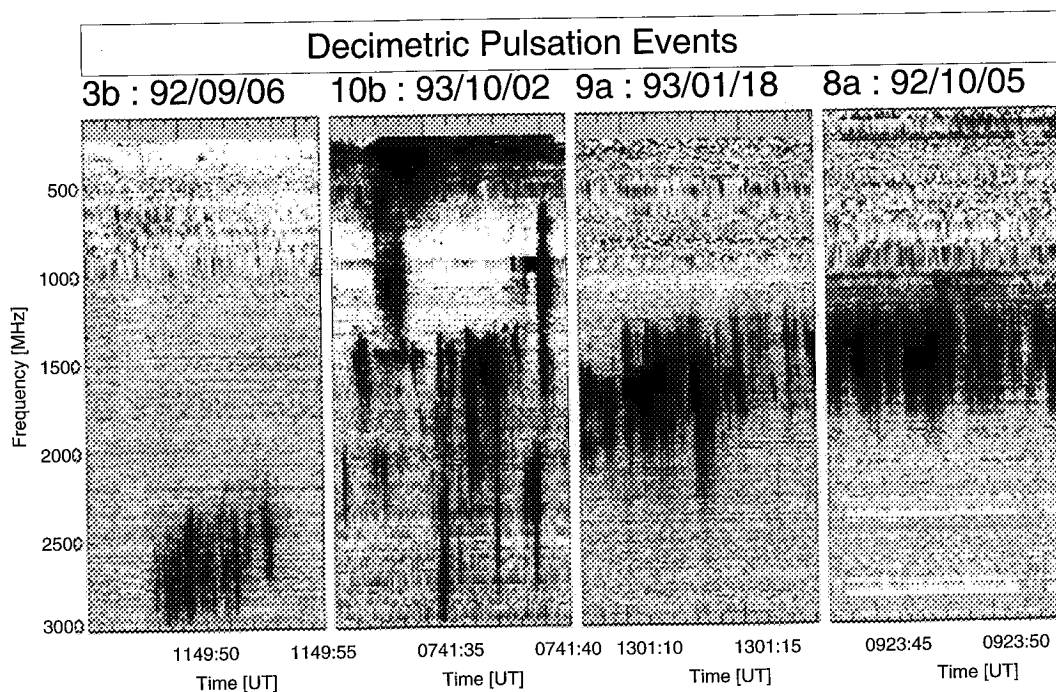


FIG. 5.—Four decimetric pulsation events, in a similar representation as Fig. 4

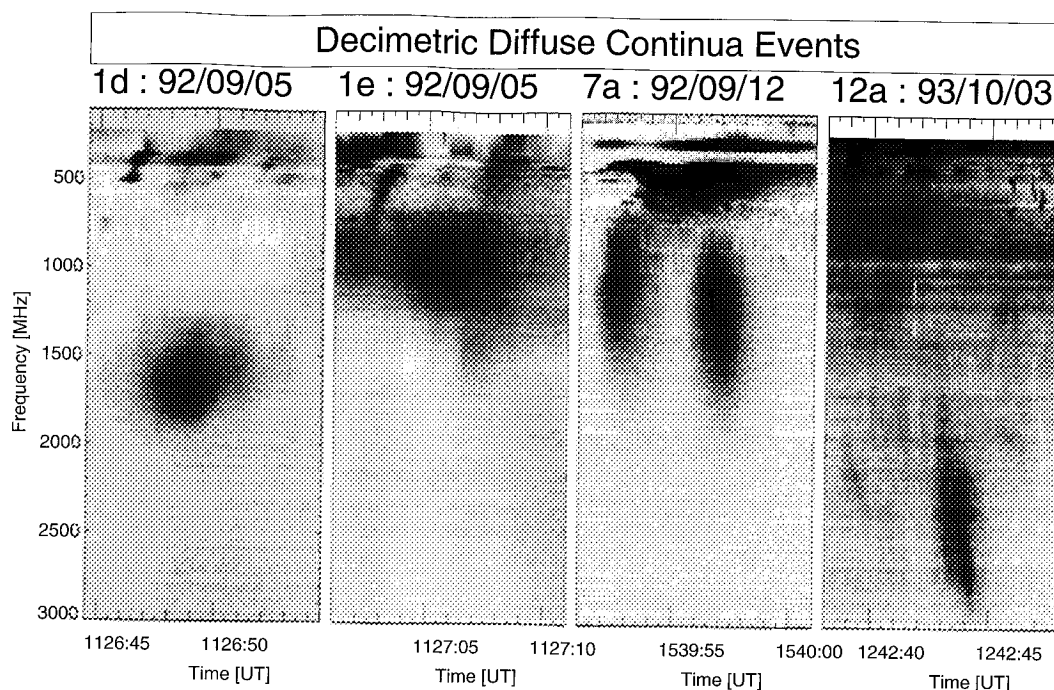


FIG. 6.—Four decimetric diffuse continua events, in a similar representation as Fig. 4

aged SXR emission measures $\langle n_e^2 dV \rangle$. On the other hand, filling factors near unity have been reported. Culhane et al. (1994) estimated a loop filling factor of 0.7 by comparing the densities inferred from the SXR emission measure ($n_e = 2.5 \times 10^{11} \text{ cm}^{-3}$) and from the conductive loss curve ($n_e = 3.6 \times 10^{11} \text{ cm}^{-3}$). Good agreement has also been found between the electron densities measured from both emission measure and line ratio methods using EUV lines (Widing & Spicer 1980).

In summary, electron densities in flare loops have been reported to cover a wide range, from $n_e \approx 10^{10}$ to $n_e \approx 10^{13} \text{ cm}^{-3}$. This large range cannot entirely be attributed to unknown filling factors, since filling factor-independent methods alone yield low values (e.g., with the plasma frequency method) as well as large values (e.g., with the SXR line ratio technique). Therefore the large variation of densities seems to be real. However, systematic differences may arise between different flare types or flare phases. Higher densities probably occur for compact, impulsive flares at flare maximum while lower densities occur for larger, longer duration flares or during flare decay periods. Another systematic difference may arise from different spatial locations. SXR line ratio techniques are perhaps most susceptible to the hottest flare plasma that flows up through the footpoints with small cross sections in chromospheric heights, where it is not properly resolved by SXT, with a resolution of $2''.5$. In contrast, SXT is perhaps more susceptible to the bulk of the evaporated plasma in the coronal part of the loop, where the electron temperature has already dropped (by a factor of ≈ 2). The radio method, on the other hand, probes a very localized interface where downward-moving electron beams intersect with the upflowing evaporation front, which is probably neither the densest nor the hottest location of a flare loop. We like to emphasize that all these considerations should be taken into account when comparing flare densities with different methods.

3.2. Radio Density Diagnostics

Our density diagnostic in the radio band is based on the electron plasma frequency, which is a direct function of the electron density and does not depend on the plasma temperature, the filling factor, or the spatial resolution of the instrument, as is the case for SXR-based density measurements using the SXR emission measure. Therefore the plasma frequency represents a very accurate tool for probing the electron density. The only ambiguity to be decided is whether an observed radio burst is produced by the plasma emission mechanism, and whether radiation is emitted at the fundamental or harmonic level. It has long been established that fast-drifting radio bursts (type III and RS) in the metric and decimetric frequency range are caused by radiation from plasma oscillations excited by electron beams (Wild, Roberts, & Murray 1954), with typical exciter velocities of $v_B/c = 0.07$ – 0.25 (Dulk et al. 1987). The question whether fundamental or harmonic plasma emission dominates for decimetric fast-drifting bursts is less clear, but the assumption of harmonic emission would decrease the values of radio-inferred densities by a factor of 4 and thus would produce larger discrepancies from the SXR-inferred density values.

Besides decimetric type III and RS bursts, for which plasma emission can be considered as established, we also identified a considerable number of decimetric pulsations and diffuse continua events, for which the radiation mechanism is not yet identified. Possible emission mechanisms are related to the gyration of trapped electrons in the magnetic field and their loss-cone distribution in velocity space (for a recent overview, see Benz 1993). Because all decimetric bursts analyzed here have timescales of $\lesssim 1$ s, or $\lesssim 2$ s for diffuse continua (see Figs. 4–6), they are produced by a coherent emission mechanism, in contrast to incoherent gyrosynchrotron emission, which has longer time structures

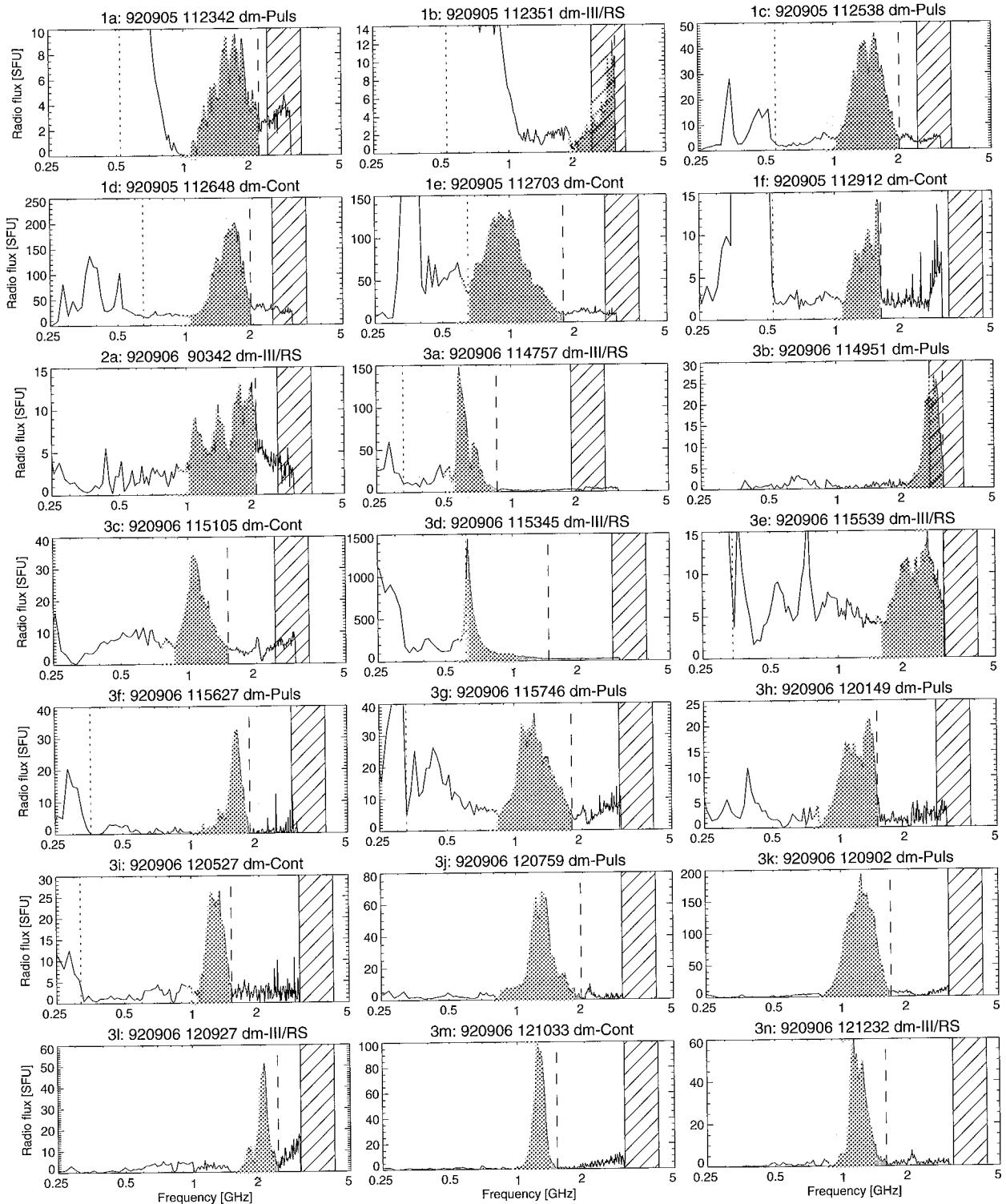


FIG. 7.—Radio spectra of the 44 analyzed events in the frequency range 0.25–3 GHz. The x-axis denotes the logarithmic frequency, the y-axis the radio flux on a linear scale in solar flux units, after subtraction of a background. The frequency range of the decimetric bursts is indicated with gray shading, and the high-frequency cutoff with a dashed line. The type III start frequencies are indicated by dotted lines. The range of plasma frequencies that corresponds to the electron density in the SXR flare loop is indicated with a hatched area, bound by the half and peak values of the SXR density n_e^{SXR} . Note that the plasma frequency of the SXR loop is generally higher than that of the decimetric radio bursts.

(≥ 5 s), peaks at higher frequencies (≥ 5 GHz), and exhibits more broadband spectra (Benz & Tarnstrom 1976). Any contribution of the relatively slowly varying gyrosynchrotron spectrum would be largely subtracted out in the

spectra shown in Figure 7, based on our preburst background subtraction. Without need to specify the emission mechanism for decimetric radio bursts, we can rely on the fact that any escaping radiation has to be emitted above the

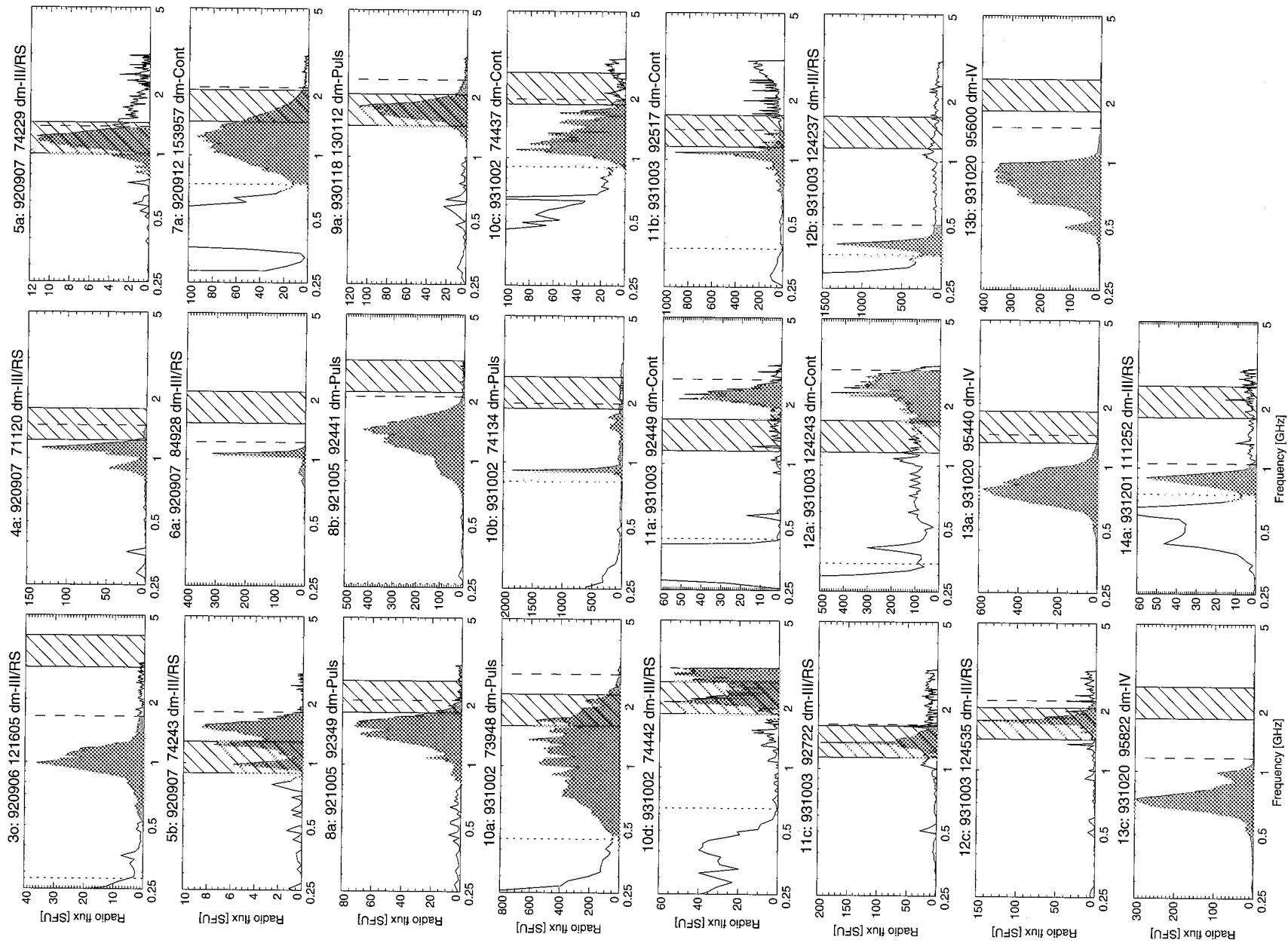


FIG. 7.—Continued

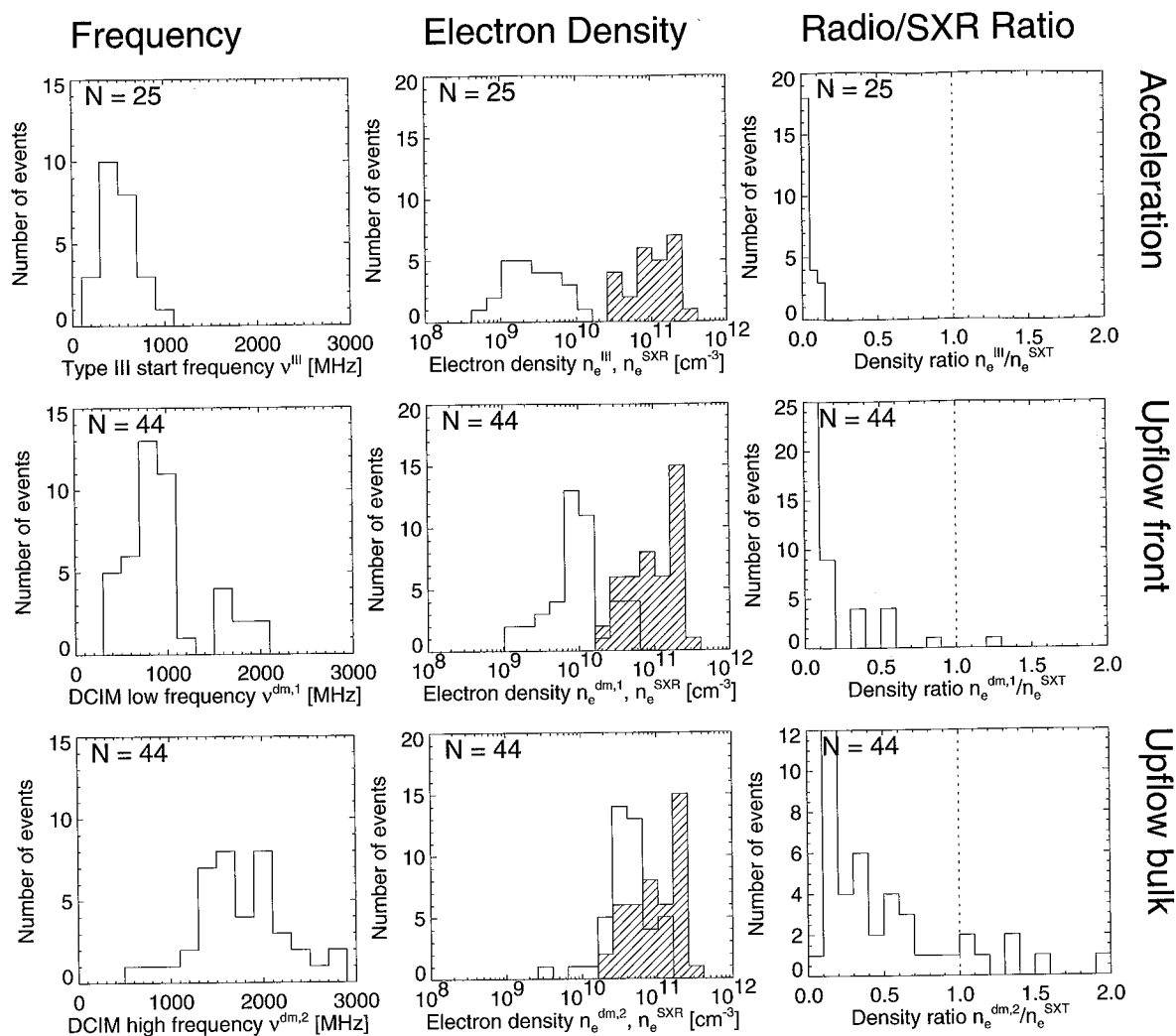


FIG. 8.—Statistics of radio frequencies (left column), electron densities (middle column), and the ratio of radio-inferred to SXR-inferred densities (right column). The open histograms refer to the radio-inferred values, the hatched histograms to the SXR-inferred values. The values are measured at the start frequency of metric type III bursts (top row), at the low frequency of decimetric bursts (middle row), and at the high frequency of decimetric bursts (bottom row). The frequency regimes of the three rows are identified with the locations of the acceleration site (top), the front (middle), and bulk (bottom) of the plasma upflow driven by the chromospheric evaporation process (see text).

local plasma frequency, and thus our density diagnostic employing the fundamental plasma frequency provides an upper limit on the local electron density in the observed radio source.

3.3. Chromospheric Evaporation

The interpretation of decimetric radio bursts has been significantly advanced by the discovery that the chromospheric evaporation process plays a fundamental role in the opacity of decimetric radio bursts (Aschwanden & Benz 1995). This effect can be simply characterized with the temperature and density dependence of the free-free opacity, i.e., $\tau_{ff} \propto n_e^2 T^{-3/2} \nu^{-2} H$ (with H the density scale height in the evaporation front, assumed to be constant in the following discussion), which reduces to $\tau_{ff} \propto n_e T^{-3/2} H$ for plasma emission. Model calculations of decimetric spectra indicate that the low-frequency cutoff is governed by the temperature increase at the evaporation front while the high-frequency cutoff is dominated by the density increase inside and behind the evaporation front (Aschwanden & Benz 1995). Since the temperature gradient at the chromospheric evaporation front changes by about a factor of $T_F/T_C \approx$

15 MK/1.5 MK = 10 from a coronal value $T_C = 1.5$ MK above the evaporation front to a flare temperature of $T_F \approx 15$ MK behind the front, the free-free opacity of plasma emission changes abruptly by a factor of $10^{3/2} \approx 30$, which constitutes a sharp low-frequency cutoff for decimetric radio bursts. In our study, this low-frequency cutoff is measured at plasma densities of $n_e^{\text{upflow},1} \equiv n_e^{\text{dm},1} = (0.13\text{--}5.1) \times 10^{10} \text{ cm}^{-3}$. Behind the chromospheric evaporation front, the electron density increases steadily because of the overpressure and thus increases the free-free opacity according to the $\tau_{ff} \propto n_e$ dependence. This opacity increase behind the evaporation front is manifested as a high-frequency cutoff for decimetric bursts, often exhibiting a slow drift toward lower frequencies due to the upward motion of the evaporation front. In our analysis, we detect this high-frequency cutoff at plasma densities of $n_e^{\text{upflow},2} \equiv n_e^{\text{dm},2} = (0.3\text{--}11.2) \times 10^{10} \text{ cm}^{-3}$. The density jump between the front and the back of the chromospheric evaporation front is found to have a typical (median) value of $Q^{\text{upflow}} = n_e^{\text{upflow},2}/n_e^{\text{upflow},1} = 3.6$. This value is consistent with hydrodynamic simulations of chromospheric evaporation upflows (Reale & Peres 1995; Mariska, Emslie, & Li 1989).

The opacity effects of the chromospheric evaporation process change the propagation conditions of all decimetric radio bursts emitted near the plasma frequency in a similar way, regardless of whether their fine structure consists of decimetric type III's, decimetric pulsations, or decimetric diffuse continua. Numerical calculations of the resulting radio brightness spectra have shown that plasma emission at the fundamental level fits the observed spectra better than emission at the harmonic level (Aschwanden & Benz 1995). In Figure 9, we show calculations of the free-free opacity for fundamental plasma emission as a function of the electron density n_e and the plasma depth r . For the temperature dependence, we assume a steady increase from the quiet coronal value of $T_C = 1.5$ MK at the upflow front (at a density of $n_e^{\text{upflow},1} = 3 \times 10^9 \text{ cm}^{-3}$) to a typical flare temperature of $T_F = 15$ MK behind the upflow front (at a density of $n_e^{\text{upflow},2} = 10^{11} \text{ cm}^{-3}$). The contours in Figure 9 indicate the parameter space $\tau_{\text{ff}}(n_e, r)$ where the free-free opacity changes from $\tau_{\text{ff}} = 1$ to $\tau_{\text{ff}} = 20$ for fundamental plasma emission. To test whether this model can explain the

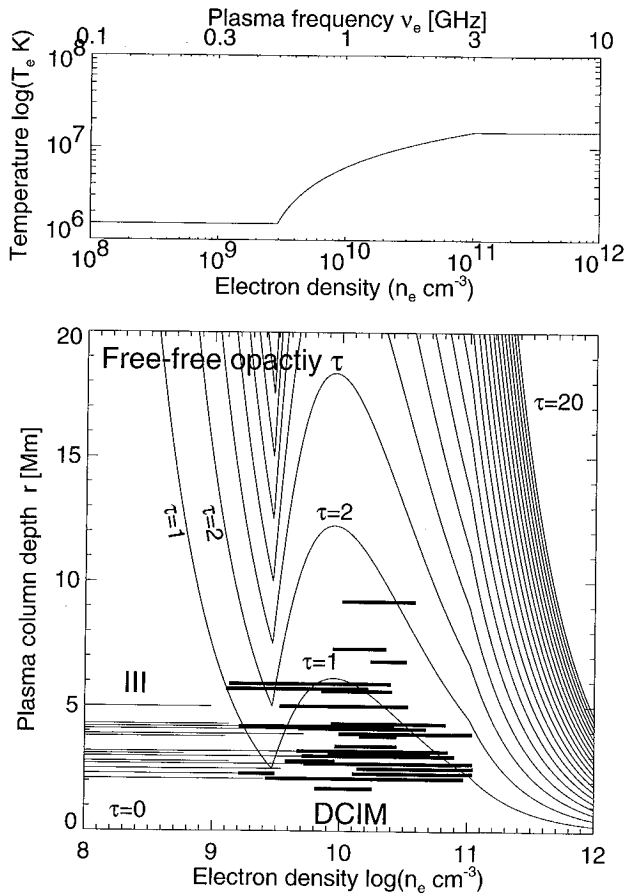


FIG. 9.—Free-free opacity $\tau_{\text{ff}}(n_e, r)$ as function of the electron density n_e and plasma column depth r at the plasma frequency, in the form of contours in two-parameter space (n_e, r) in the bottom panel (with contour levels $\tau_{\text{ff}} = 1, 2, \dots, 20$). The plasma is assumed to be of coronal temperature ($T_C = 1.5$ MK) for low densities ($n_e \leq 3 \times 10^9 \text{ cm}^{-3}$), of flare temperature ($T_F = 15$ MK) for high densities ($n_e \geq 10^{11} \text{ cm}^{-3}$), and is linearly interpolated for intermediate values (top). The observed 44 decimetric burst (“DCIM”) episodes (thick lines) and 25 metric type III (“III”) bursts (thin lines) are inserted in the bottom panel according to the radio-inferred densities and with a plasma column depth estimated from the SXR loop radius. Note that all radio bursts are domiciled in optically thin regimes, with $\tau_{\text{ff}} \lesssim 1$.

observability of decimetric bursts, we place each of the 44 events onto this diagram, according to the density inferred from their plasma frequency and the plasma depth r estimated from the SXR loop radius $r = d/2$. From this averaged opacity diagram, we see that all decimetric bursts are indeed emitted under conditions in which the corona is sufficiently transparent ($\tau_{\text{ff}} \lesssim 1$). Although we do not know the intrinsic brightness temperature T_B of decimetric radio bursts, since all we observe is $T_B^{\text{obs}} = T_B e^{-\tau}$, it is safe to assume that high opacities of $\tau_{\text{ff}} \gtrsim 10$ would completely suppress them. The diagram in Figure 9 also demonstrates clearly that the decimetric bursts are visible only because of the high flare temperature (see the reduced free-free opacity at $n_e \gtrsim 3 \times 10^{10} \text{ cm}^{-3}$ in Fig. 9, bottom, caused by the temperature increase $T_e \gtrsim 2 \text{ MK}$ in Fig. 9, top), but they would be completely absorbed at a quiet coronal temperature.

The decimetric spectra can be directly compared with the plasma frequency of the SXR-bright flare loop (see Fig. 7). Although the plasma frequency corresponding to electron densities in SXR flare loops is close to the highest frequency (3.0 GHz) observable by Phoenix, there is in most of the observed cases no evidence that the spectrum of decimetric bursts extends beyond the plasma frequency observed in the SXR loop. The low-frequency cutoff of decimetric bursts is found to be lower than the SXR plasma frequency in 98% of the cases (Fig. 8, middle right), and the high-frequency cutoff of decimetric bursts is also found to be lower than the SXR plasma frequency in 84% of the cases (Fig. 8, bottom right). If we take the ratio of the radio-inferred electron densities to the SXR-inferred values, we find ratios of $q^{\text{upflow},1} = n_e^{\text{dm},1}/n_e^{\text{SXR}} = 0.016\text{--}1.27$ (with a median value of 0.09) for the upflow front, and ratios of $q^{\text{upflow},2} = n_e^{\text{dm},2}/n_e^{\text{SXR}} = 0.09\text{--}3.05$ (with a median value of 0.35) behind the upflow front, in the bulk part of the upflowing plasma (Table 2). Thus we infer that the filled loops have on average a peak density ≈ 3 times higher than the upflowing plasma. Numerical hydrodynamic simulations (Reale & Peres 1995) indeed show a density jump of about a factor of 3 in the upflowing front, as well as an additional overall density increase by a factor of 3 on timescales of 20–60 s after the upflow front reaches the apex of the loop. This temporal evolution of the filling process has to be translated into a spatial picture, where new loops subsequently start to fill up after the filling of earlier loops is completed. In the magnetic reconnection scenario this is a natural evolution, since the magnetic reconnection X-point proceeds to higher altitudes during the impulsive phase of flares (Kopp & Pneuman 1976), which gradually separates the topologically connected footpoints, where precipitating electrons heat the chromosphere and drive chromospheric evaporation in a gradually expanding footpoint area. This flare scenario and its relation to decimetric radio bursts are depicted in Figure 10 (see also the numerical simulations of magnetic reconnection for this scenario by Magara et al. 1996). An identification of chromospheric evaporation in simultaneous SXR and radio images was recently attempted by Silva et al. (1997).

3.4. The Acceleration Site

The type III frequencies range between 220 and 910 MHz, corresponding to electron densities of $n_e^{\text{III}} = 0.6 \times 10^9$ to $1.0 \times 10^{10} \text{ cm}^{-3}$ for the case of fundamental plasma emission. The significance of type III start frequencies is that they demarcate the electron density in the acceleration

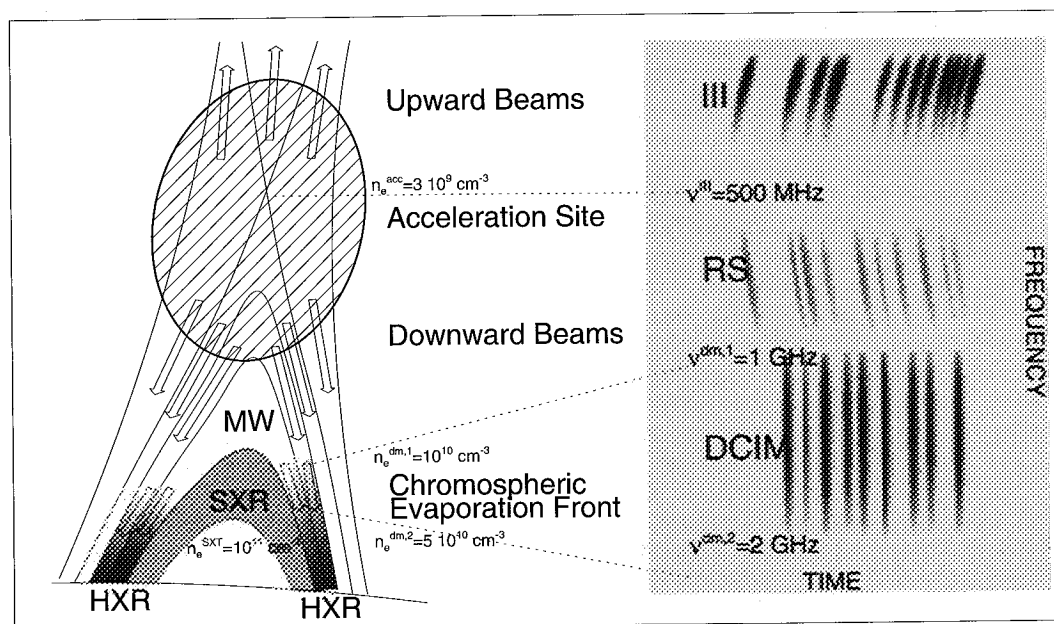


FIG. 10.—Diagram of a flare model envisioning magnetic reconnection and chromospheric evaporation processes in the context of our electron density measurements. The panel on the right illustrates a dynamic radio spectrum with radio bursts indicated in the frequency-time plane. The acceleration site is located in a low-density region (in the cusp) with a density of $n_e^{\text{acc}} \approx 10^9 \text{ cm}^{-3}$ from where electron beams are accelerated in upward (type III) and downward (RS bursts) directions. Downward-precipitating electron beams that intercept the chromospheric evaporation front with density jumps over $n_e^{\text{upflow}} = (1-5) \times 10^{10} \text{ cm}^{-3}$ can be traced as decimetric bursts with almost infinite drift rate in the 1–2 GHz range. The SXR-bright flare loops completely filled up by evaporated plasma have somewhat higher densities of $n_e^{\text{SXR}} \approx 10^{11} \text{ cm}^{-3}$. The chromospheric upflow fills loops subsequently with wider footpoint separation while the reconnection point rises higher.

region. The type III and RS bursts identified here occur during the main impulsive flare phase, and their detailed correlation with HXRs was established in several recent studies (e.g., Aschwanden et al. 1993, 1995). It was not known in earlier studies whether the start frequency of metric type III bursts would be significantly displaced to lower frequencies than the plasma frequency of the acceleration region, because a minimal propagation distance is needed for electron beams to become unstable (Kane, Benz, & Treumann 1982). However, recent studies of the starting point of combined upward- and downward-propagating beam signatures (see bidirectional type III + RS burst pairs in Aschwanden et al. 1995, 1993; Klassen 1996) demonstrated that the centroid position of the acceleration region is close to the start frequency of strong type III bursts. The only major difficulty with this scenario is the observed asymmetry of electron numbers accelerated in the upward/downward direction, which was inferred to be as low as 10^{-2} to 10^{-3} , comparing the electrons detected in interplanetary space with those required to satisfy the chromospheric thick-target HXR emission (Lin 1974). It is not clear whether this asymmetry can be explained by the dominance of closed magnetic field lines above acceleration regions. In the following discussion, we associate the start frequency ν^{III} of type III bursts with the electron density n_e^{acc} in the acceleration region. The range of type III start frequencies (220–910 MHz) measured here is found to be nearly identical with that (270–950 MHz) of 30 bidirectional III + RS burst pairs analyzed in Aschwanden et al. (1995). Comparing these densities in the acceleration region with those in the SXR-bright flare loop, we find very low ratios of $n_e^{\text{acc}}/n_e^{\text{SXR}} = 0.007\text{--}0.127$ (with a median of 0.027), i.e., the density in the acceleration region is 1–2 orders of magnitude lower than in the SXR-bright flare loop.

This result has dramatic consequences for the location of the acceleration site. The extremely low density ratio in the acceleration site found in all flares, without exception, leaves no room to place the acceleration site inside the SXR-bright flare loop (assuming a filling factor near unity). If we were to allow for harmonic plasma emission or for nonunity filling factors of the SXR loop, the density ratio between the acceleration site and the SXR loop would be even more extreme. Therefore we see no other possibility than to conclude that the acceleration site is located outside the SXR-bright flare loop. The next question is the magnetic topology that can accommodate such large density gradients ($\sim 2\text{--}5$ density scale heights). A possible topology is a cusp-shaped magnetic field geometry above the SXR-bright flare loop, where acceleration is assumed to take place beneath the X- or Y-type magnetic reconnection point (see diagram in Fig. 10; for a detailed physical model, see Tsuneta 1996). The magnetic field lines that connect the cusp with the footpoints can have arbitrarily lower densities than the encompassed closed field lines that have been filled by evaporated plasma. Of course, the high density gradient between the acceleration site and the filled SXR-bright flare loops can only be maintained in a dynamical process in which the reconnection point proceeds to higher altitudes (Kopp & Pneuman 1976) before chromospheric evaporation has filled up the cusp volume. This race of the reconnection point with the evaporation front in the upward direction may come to a halt in long-duration flares, where the cusp volume becomes clearly filled up (Tsuneta et al. 1992; Forbes & Acton 1995).

This flare scenario, in which acceleration takes place in a low-density region above the much denser SXR-bright flare loop, would predict a physical separation between non-thermal and thermal electrons. While the SXR-bright flare

loop is entirely filled with a thermal (≈ 15 MK) plasma that is fully collisional, the low-density region above the SXR-bright flare loop, which encompasses the acceleration site in the cusp region, is essentially collisionless and partially traps the accelerated nonthermal particles by magnetic mirroring. The confined nonthermal particles may also represent the source of gyrosynchrotron emission observed in microwaves. This is consistent with the electron densities (of the thermal plasma) inferred in microwave sources, which are generally lower ($n_e \lesssim$ a few times 10^{10} cm^{-3} ; see the compilation in Bray et al. 1991, p. 245; Dulk, Bastian, & Kane 1986; Bastian & Gary 1992; Kucera et al. 1993; Gary et al. 1996) than in the SXR-bright flare loops ($n_e \approx 10^{11} \text{ cm}^{-3}$). On the other hand, chromospheric evaporation occurs most efficiently at chromospheric footpoints that are heated by precipitated electrons, e.g., from the loops that are connected with the acceleration region and are trapping microwave-emitting, highly relativistic electrons. The evaporation at the footpoints of such microwave-emitting loops then suppresses gyrosynchrotron emission there by the Razin effect, which was found to operate at typical densities of $n_e \approx 2 \times 10^{11}$ (Belkora 1995), as found similarly for our decimetric high-frequency cutoffs $n_e^{\text{dm},2}$. Electron time-of-flight measurements from HXR data clearly indicate that the acceleration site is located a factor of 1.6 ± 0.4 higher than the apex of the SXR loop (Aschwanden et al. 1996b). An additional argument for the location of the acceleration site outside the dense SXR-bright flare loops is also the collisional lifetime of ≥ 20 keV electrons, which would be stopped inside the dense ($n_e^{\text{SXR}} \gtrsim 10^{11} \text{ cm}^{-3}$) SXR-bright loop before they could reach the footpoints, where non-thermal ≥ 20 keV HXR emission is often observed.

4. CONCLUSIONS

In this study, we compared electron density measurements from radio and SXR observations of solar flare loops. The electron densities inferred from radio bursts make use of the fundamental plasma frequency, which is believed to represent the approximate observed frequency for most fast-drifting metric and decimetric radio bursts. Since we make use of broadband dynamic spectra over the frequency range 0.1–3 GHz (from Phoenix), we are sensitive to electron densities from about $n_e = 10^8$ to $n_e \approx 10^{11} \text{ cm}^{-3}$. The electron densities inferred from SXR images are based on measurements of the line-of-sight emission measure and estimates of the column depth by measuring the loop diameters perpendicular to the line of sight. Comparing the densities inferred from these two methods in an unbiased sample of 44 flare episodes during 14 commonly observed flares, we arrive at the following conclusions:

1. The electron density in the *acceleration site* that separates upward- and downward-accelerated electron beams, probed by the plasma frequency of type III and RS bursts, has a density of $n_e^{\text{acc}} = (0.6\text{--}10) \times 10^9 \text{ cm}^{-3}$, which is

only a few percent of that in the SXR-bright flare loop, and thus must be located significantly outside the SXR-bright flare loop, probably in the cusp region above the SXR flare loop. This conclusion is consistent with the scaling law between electron time-of-flight distances and flare loop lengths (Aschwanden et al. 1996a, 1996b) and could also provide an explanation for the HXR sources above the loop top (Masuda 1994).

2. Upflowing plasma driven by the *chromospheric evaporation* process can be detected by means of decimetric radio bursts as a consequence of opacity effects of free-free absorption. We find electron densities of $n_e^{\text{upflow},1} = (0.1\text{--}5) \times 10^{10} \text{ cm}^{-3}$ at the upflow front and about a factor of 3.6 higher behind the front, where decimetric bursts become completely absorbed. These densities amount to 10%–30% of completely filled loops, for which we measure densities of $n_e^{\text{SXR}} = (0.2\text{--}2.5) \times 10^{11} \text{ cm}^{-3}$ in SXRs. The comparison of radio and SXR density diagnostics seems to be satisfactory, considering the fact that radio bursts are sensitive to upflowing plasma while the SXR peak emission measure refers to the brightest loops, after they have been filled up.

This study has demonstrated, for the first time, that radio and SXR measurements provide fully compatible electron density measurements. Furthermore, the combined use of both methods conveys complementary information that leads to powerful constraints for flare scenarios and the localization of particle acceleration sites that would not be possible with either method alone. In future work we plan to refine the radio diagnostic further, with spectral modeling of decimetric bursts, which potentially allows us to determine the electron density and temperature simultaneously in upflowing plasmas.

We gratefully acknowledge helpful discussions and comments from Hugh Hudson, Takeo Kosugi, Kuniko Hori, Stephen White, and from the referee, Ken Phillips. The *Yohkoh* data used in this paper were provided by the *Yohkoh* mission of ISAS, Japan, which was prepared and is operated by an international collaboration of Japanese, US, and UK scientists under the support of ISAS, NASA, and PPARC, respectively. Magnetogram data from NSO/Kitt Peak used here are produced cooperatively by NSF/NOAO, NASA/GSFC, and the NOAA Space Environment Laboratory. The Solar Data Analysis Center at GSFC, managed by J. Gurman, is acknowledged for providing computational and database facilities. We thank Rita Johnson for assisting with the *Yohkoh* data. The Phoenix data were made accessible with software developed by André Csillaghy. We thank Werner Stehling and his team for operation of the Zurich radio spectrometers. Construction and operation of the Zurich radio spectrometers is supported by the Swiss National Science Foundation (grant 20-46656.96). The work of M. J. A. was supported by NASA grant NAGW-4581.

REFERENCES

- Aschwanden, M. J., & Benz, A. O. 1995, *ApJ*, 438, 997
 Aschwanden, M. J., Benz, A. O., Dennis, B. R., & Schwartz, R. A. 1995, *ApJ*, 455, 347
 Aschwanden, M. J., Benz, A. O., & Schwartz, R. A. 1993, *ApJ*, 417, 790
 Aschwanden, M. J., Kosugi, T., Hudson, H. S., Wills, M. J., & Schwartz, R. A. 1996a, *ApJ*, 470, 1198
 Aschwanden, M. J., Wills, M. J., Hudson, H. S., Kosugi, T., & Schwartz, R. A. 1996b, *ApJ*, 468, 398
 Bastian, T. S., & Gary, D. E. 1992, *Sol. Phys.*, 139, 357
 Belkora, L. A. 1995, Ph.D. thesis, Univ. Colorado
 Benz, A. O. 1993, *Plasma Astrophysics: Kinetic Processes in Solar and Stellar Coronae* (Dordrecht: Kluwer)
 Benz, A. O., Güdel, M., Isliker, H., Miszkowicz, S., & Stehling, W. 1991, *Sol. Phys.*, 133, 385
 Benz, A. O., & Tarnstrom, G. L. 1976, *ApJ*, 204, 597
 Bray, R. J., Cram, L. E., Durrant, C. J., & Loughhead, R. E. 1991, *Plasma Loops in the Solar Corona* (Cambridge: Cambridge Univ. Press)
 Brown, J. C., & Nakagawa, Y. 1978, *ApJ*, 225, L153

- Brown, W. A., Bruner, M. E., Acton, L. W., & Mason, H. E. 1986, *ApJ*, 301, 981
- Culhane, J. L., Phillips, A. T., Kosugi, T., Inada-Koide, M., & Pike, C. D. 1994, in *Proc. Kofu Symp.*, ed. S. Enome & T. Hirayama (NRO Rep. 360) (Minamisaku: Nobeyama Radio Obs.), 117
- Ding, M. D., Watanabe, T., Shibata, K., Sakurai, T., Kosugi, T., & Fang, C. 1996, *ApJ*, 458, 391
- Doschek, G. A. 1990, *ApJS* 73, 117
- . 1994, in *Proc. Kofu Symp.*, ed. S. Enome & T. Hirayama (NRO Rep. 360) (Minamisaku: Nobeyama Radio Obs.), 173
- Doschek, G. A., Feldman, U., Landecker, P. B., & McKenzie, D. L. 1981, *ApJ*, 249, 372
- Doschek, G. A., Strong, K. T., & Tsuneta, S. 1995, *ApJ*, 440, 370
- Dulk, G. A., Bastian, T. S., & Kane, S. R. 1986, *ApJ*, 300, 438
- Dulk, G. A., Steinberg, J. L., Hoang, S., & Goldman, M. V. 1987, *A&A*, 173, 366
- Fisher, R. R. 1974, *Sol. Phys.*, 35, 401
- Forbes, T. G., & Acton, L. W. 1995, *ApJ*, 459, 330
- Foukal, P., Miller, P., & Gilliam, L. 1983, *Sol. Phys.*, 83, 83
- Gabriel, A. H., & Jordan, C. 1972, in *Case Studies in Atomic Collision Physics*, Vol. 2, ed. E. W. McDaniel & M. C. McDowell (Amsterdam: North-Holland), 209
- Gary, D. E., Wang, H., Nitta, N., & Kosugi, T. 1996, *ApJ*, 464, 965
- Güdel, M., & Benz, A. O. 1988, *A&AS*, 75, 243
- Ichimoto, K., Hirayama, T., Yamaguchi, A., Kumagai, K., Tsuneta, S., Hara, H., Acton, L. W., & Bruner, M. E. 1992, *PASJ*, 44, L117
- Islaker, H., & Benz, A. O. 1994, *A&AS*, 104, 145
- Kane, S. R., Benz, A. O., & Treumann, R. A. 1982, *ApJ*, 263, 423
- Klassen, A. 1996, *Sol. Phys.*, 167, 449
- Kopp, R. A., & Pneuman, G. W. 1976, *Sol. Phys.*, 50, 85
- Kucera, T. A., Dulk, G. A., Kiplinger, A. L., Winglee, R. M., Bastian, T. S., & Graeter, M. 1993, *ApJ*, 412, 853
- Lin, R. P. 1974, *Space Sci. Rev.*, 16, 189
- Linford, G. A., & Wolfson, C. J. 1988, *ApJ*, 331, 1036
- Magara, T., Mineshige, S., Yokoyama, T., & Shibata, K. 1996, *ApJ*, 466, 1054
- Mariska, J. T., Emslie, A. G., & Li, P. 1989, *ApJ*, 341, 1067
- Martens, P. C., Acton, L. W., & Lemen, J. R. 1995, *Sol. Phys.*, 157, 141
- Masuda, S. 1994, Ph.D. thesis, Univ. Tokyo
- McKenzie, D. L., Broussard, R. M., Landecker, P. B., Rugge, H. R., & Young, R. M. 1980, *ApJ*, 238, L43
- Mewe, R., Gronenschild, E. H. B. M., & van den Oord, G. H. J. 1985, *A&AS*, 62, 197
- Mewe, R., Lemen, J. R., & van den Oord, G. H. J. 1986, *A&AS*, 63, 511
- Morrison, M. 1994, *Yohkoh Analysis Guide* (version 2.00; Palo Alto, CA: Lockheed Palo Alto Res. Lab.)
- Pallavicini, R., Serio, S., & Vaiana, G. S. 1977, *ApJ*, 216, 108
- Phillips, K. J. H. 1991, *Phil. Trans. R. Soc. A*, 336, 461
- Phillips, K. J. H., Bhatia, A. K., Mason, H. E., & Zarro, D. M. 1996, *ApJ*, 466, 549
- Reale, F., & Peres, G. 1995, *A&A*, 299, 225
- Silva, A. V. R., Wang, H., Gary, D. E., Nitta, N., & Zirin, H. 1997, *ApJ*, in press
- Simnett, G. M., & Benz, A. O. 1986, *A&A*, 165, 227
- Tsuneta, S. 1996, *ApJ*, 456, 840
- Tsuneta, S., et al. 1991, *Sol. Phys.*, 136, 37
- Tsuneta, S., Hara, H., Shimizu, T., Acton, L. W., Strong, K. T., Hudson, H. S., & Ogawara, Y. 1992, *PASJ*, 44, L63
- Widing, K. G., & Spicer, D. S. 1980, *ApJ*, 242, 1243
- Wiehl, H. J., Benz, A. O., & Aschwanden, M. J. 1985, *Sol. Phys.*, 95, 167
- Wild, J. P., Roberts, J. A., & Murray, J. D. 1954, *Nature*, 173, 532
- Zarro, D. M., Mariska, J. T., & Dennis, B. R. 1994, in *Proc. Kofu Symp.*, ed. S. Enome & T. Hirayama (NRO Rep. 360) (Minamisaku: Nobeyama Radio Obs.), 221

